Corrosion Science 219 (2023) 111210

Contents lists available at ScienceDirect

Corrosion Science

journal homepage: www.elsevier.com/locate/corsci

Evaluation of microstructural and environmental effects on the hydrogen uptake and desorption in high-strength carbon steels: A thermal desorption spectroscopy study

Shabnam Karimi [a,*], Iman Taji [a], Simona Palencsár [b], Arne Dugstad [b], Tarlan Hajilou [a], Afrooz Barnoush [a,c], Kim Verbeken [d], Roy Johnsen [a], Tom Depover [d]

[a] Department of Mechanical and Industrial Engineering, Norwegian University of Science and Technology (NTNU), N-7491 Trondheim, Norway
[b] Institute for Energy Technology (IFE), P.O. Box 40, NO-2027, Kjeller, Norway
[c] Qatar Environment and Energy Research Institute (QEERI), Hamad Bin Khalifa University (HBKU), P.O. Box 34110, Doha, Qatar
[d] Department of Material, Textiles and Chemical Engineering, Ghent University (UGent), Technologiepark 46, B-9052 Ghent, Belgium

ARTICLE INFO

Keywords:
Thermal desorption spectroscopy
Carbon steel
CO_2 environment
CO_2/H_2S environment
Pearlite
Spheroidite

ABSTRACT

The hydrogen uptake in three high-strength carbon steels is studied after exposure to three different environments: an aqueous solution with CO_2 bubbling, CO_2/H_2S bubbling, and cathodic charging without external gassing. The hydrogen uptake is substantially higher in CO_2/H_2S environment compared to CO_2 environment for all materials. The lamellar cementite morphology absorbs higher hydrogen than the material with spheroidite microstructure with similar carbon content. The corrosion layer formed on the steels in CO_2 environment strongly affects the hydrogen effusion and the thermal desorption spectroscopy spectrum in all materials, while the corrosion layer formed in CO_2/H_2S environment does not show this effect.

1. Introduction

Flexible pipes are key components in offshore oil and gas fields. Their role is to transport the hydrocarbons, fluids, and gas between the production facilities and the subsea installations. They are composed of several metallic and polymeric layers and their structure is illustrated in other studies [1,2]. Carbon steels have a strong position in flexible pipe production due to their excellent mechanical properties, availability, and cost [3]. The carbon steels that are used in flexible pipes are subjected to tension and compression and are prone to failure [2]. Therefore, the potential hydrogen embrittlement of flexible pipe carbon steels is a key factor that should be considered in material selection.

A very corrosive environment can develop in the annulus space of a flexible pipe due to the entry of chemical species like CO_2 and H_2S along with water into the annulus. CO_2 can generate carbonic acid in the brine and accelerate the corrosion process [4,5]. Previous studies showed that steels are susceptible to environmentally assisted cracking due to the presence of CO_2 in a saline environment [6–8]. The detrimental effect of CO_2 is less critical than in the H_2S environment for the same material. H_2S prevents the hydrogen recombination and increases the hydrogen uptake in steels [9]. Furthermore, hydrogen sulfide in an aqueous environment takes part in auto-catalytic cathodic reaction and produce more $H_{(abs)}$ on the surface of the steel [10]. The presence of H_2S along with CO_2 cause different failures like sulfide stress corrosion cracking, hydrogen induced cracking, and hydrogen embrittlement [11–14].

Both CO_2 and H_2S generate hydrogen protons (H^+) in an aqueous environment. The generated proton can corrode the surface of the steel and can also react with the electrons and produce atomic hydrogen. This atomic hydrogen permeates into the steel and can either fill the trapping sites in the material, linked to microstructural heterogeneities, or diffuse via the lattice sites [15]. These hydrogen traps are the microstructural sites with higher hydrogen affinity than the interstitial lattice sites, such as dislocations, voids, vacancies, grain boundaries, phase boundaries, carbides, and some intermetallic particles [16,17]. Therefore, besides the effect of the environment on the hydrogen uptake capacity, the microstructure of carbon steel also plays a crucial role. In a corrosive environment, not only the rate of cathodic reactions controlling the amount of hydrogen produced on the surface but also where the cathodic reaction happens on the surface of the steel is a relevant parameter [18].

In a ferrite/pearlite microstructure, the cementite (Fe_3C)/ferrite interfaces act as a trap for hydrogen [19–21]. The Fe_3C phase can also function as a cathodic site which accelerates the anodic dissolution process of the ferrite phase in a corrosive environment [22,23]. The Fe_3C

* Corresponding author.
E-mail address: shabnam.karimi@ntnu.no (S. Karimi).

https://doi.org/10.1016/j.corsci.2023.111210
Received 7 February 2023; Received in revised form 14 March 2023; Accepted 21 April 2023
Available online 4 May 2023

phase remains on the metal surface after the selective dissolution of ferrite [6]. In CO_2 environment, if the concentration of Fe^{2+} and CO_3^{2-} ions is sufficient, the iron carbonate ($FeCO_3$) can precipitate in between the remaining Fe_3C particles or layers and decrease the corrosion rate, slowing down the diffusion of ions to and from the steel surface and retard the hydrogen uptake [6,24]. Since the remaining Fe_3C functions as a mechanical anchor for the corrosion products like $FeCO_3$ to adhere to the steel surface and make a protective covering on the surface, the morphology and distribution of Fe_3C are of high importance [25]. Indeed the morphology, distribution, and fraction of Fe_3C have an important effect on hydrogen uptake whether Fe_3C is considered as a microstructural feature or a constitute of the corrosion layer. Crolet et al. [26] discussed that a lamellar remaining Fe_3C phase may induce internal acidification in the corrosion layer and inhibit the formation of $FeCO_3$ and as a result prevent the formation of a protective layer. In other studies, it has been discussed that the interlamellar spacing in a lamellar pearlite microstructure and the size of the Fe_3C particles affect the hydrogen embrittlement [27–29]. Bott et al. [30] investigated the effect of Fe_3C morphology and distribution on the hydrogen permeation parameters of a low-carbon steel. Their results verified that the changes in the Fe_3C morphology considerably affect the apparent diffusivity, solubility, and permeability of hydrogen. Ramunni et al. [31] showed similar results as Bott et al. They discussed that the fine Fe_3C increases solubility and decreases hydrogen diffusivity in their studied carbon steel, while the lamellar morphology of Fe_3C enhances the hydrogen diffusion coefficient and reduces the hydrogen solubility.

In the H_2S environment, sulfides are the main corrosion product that is formed on the steel surface. Sulfides can act as cathodic site and increase the hydrogen uptake [32]. It is also probable to decrease the hydrogen concentration on the steel surface and retard the hydrogen permeation to the steel. Wallaert et al. [33] discussed that the FeS layer forms and grows by ionic conduction of S^{2-} and HS^- which causes the release of a lot of hydrogen outside the FeS layer. The released hydrogen will be lost in the environment and therefore decrease the hydrogen permeation to the steel. Folena et al. [34] showed in their study that dependent on the H_2S concentration and test conditions, different FeS morphologies with different characteristics can form on the steel that has different effects on hydrogen permeation. Mackinawite and pyrrhotite present a weak blocking effect in their study. They discussed that the low concentrations of H_2S result in the precipitation of an inefficient and non-compact FeS film which does not have a diminishing effect on the hydrogen uptake.

Extensive studies have been performed to understand how hydrogen uptake is influenced by the microstructure and the microstructural defects' interaction with hydrogen. However, limited research has studied the influence of cementite morphologies and distribution on hydrogen uptake capacity. The role of the corrosion layers formed on the steels in the presence of the oil and gas industry chemical species like CO_2 and H_2S, on the hydrogen permeation characteristics were investigated before [6,35–38]. However, for the first time, the effect of the corrosion layers on hydrogen effusion and thermal desorption spectroscopy (TDS) is studied and discussed in this paper.

In the present work, three carbon steels with different microstructures, containing 0.62%, 0.65%, and 0.83% carbon (which are used as tensile armor wires in flexible pipes) are exposed to modified artificial seawater with CO_2 and CO_2/H_2S gas purging at open circuit. The same materials were also charged cathodically in a brine solution without external gassing. Employing TDS, the hydrogen uptake in these steels under the exposure to the three above-mentioned environments (CO_2 environment, CO_2/H_2S environment and cathodic charging condition) are studied. The effect of exposure medium, microstructures, and corrosion layers on the hydrogen desorption and TDS spectrum are discussed.

2. Experimental

2.1. Materials and sample preparations

Three carbon steels, containing 0.62, 0.65, and 0.83 wt% carbon, with different microstructures, were investigated in the current study. The studied materials' chemical compositions and mechanical properties [18,39] are listed in Table 1. The materials were received as drawn curved wires with a thickness of 3 mm and a width of 9 to 12 mm. Rectangular specimens, with a length of 12 mm and with the same width and thickness as the wires, were cut from the received wires. Three sets of specimens were prepared. For preparing the first set for corrosion tests, all surfaces were ground with 320 grit SiC paper. The second set with the same dimensions was prepared for cathodic charging. They were ground up to 2000 grit SiC papers. The samples of the third set were ground up to 4000 grit SiC papers and mechanically polished with 3 μm and 1 μm diamond suspensions for microstructural analysis in a Scanning Electron Microscope (SEM). After the grinding and polishing steps, all samples were cleaned in acetone and isopropanol in an ultrasound bath and dried.

2.2. Corrosion tests and hydrogen uptake

The corrosion experiments were conducted in a setup comprising two parts: the test cell, where the test specimens were immersed in the test electrolyte, and the refill cell, which contained the fresh electrolyte required to replenish the electrolyte in the test cell to ensure a low concentration of dissolved corrosion products like Fe^{2+}. A schematic of the corrosion test setup is shown in Fig. 1. Modified $ASTM\ D1141$-90 [40] seawater (without calcium chloride to avoid the formation of non-protective calcium carbonate ($CaCO_3$) [41]), was used as the corrosion test electrolyte. Its chemical composition is presented in Table 2. The electrolyte in both the test cell and refill cell purged with the requisite gas mixture persistently. The setup temperature was kept at 25 °C using a water bath. A gas dosing system based on Bronkhorst mass flow controllers was operated to mix the needed gas composition (N_2, CO_2, H_2S) and purge the test cell and the refill cell.

The electrolyte was circulated between the test cell and refill cell using a peristaltic pump equipped with $Tygon$ and PVC tubes. The flow rates were controlled by the tubing diameter and the rotation speed of the pump. To avoid oxygen contamination, the pump was placed in a chamber purged with N_2. When the peristaltic pump was on, the flow of liquid into the test cell was continuous and had a maximum rate of 4 ml/min (using a 1.143 mm tubing diameter). The backward flow had a maximum rate of 18 ml/min (using a 3.175 mm tubing diameter) and was self-regulated by draw-off to eliminate the risk of overflowing the test cell. The backward flow was directed to a waste container. The pH value was continuously recorded. The pH increased slightly (between 5.77 and 6.08) during both the CO_2 and CO_2/H_2S exposure experiments. The test cell electrolyte was sampled frequently during exposure to analyze its Fe^{2+} ion concentration. The Fe^{2+} ions were converted to a colored Fe complex, which was photometrically quantified. The electrolyte was continuously replaced by fresh electrolyte (with no dissolved corrosion products) at a flow rate of ca. 0.8–1.6 l/day to ensure a low concentration of Fe^{2+} (less than 80 ppm in the test cell).

Two sets of corrosion experiments were performed by purging 0.2 bar CO_2 in set number one and 0.2 bar CO_2, 1 mbar H_2S in the other set with a flow rate of 200 ml/min. In the second test set, since the precipitation of FeS kept the concentration of the dissolved Fe^{2+} ions low, no electrolyte replacement was needed. The duration of both sets of tests was 504 h (21 days). After the corrosion test, the specimens were immediately immersed in liquid nitrogen to prevent the hydrogen egress from the specimens, and also to start the TDS test with a specimen with low temperature to minimize the hydrogen loss before the test onset.

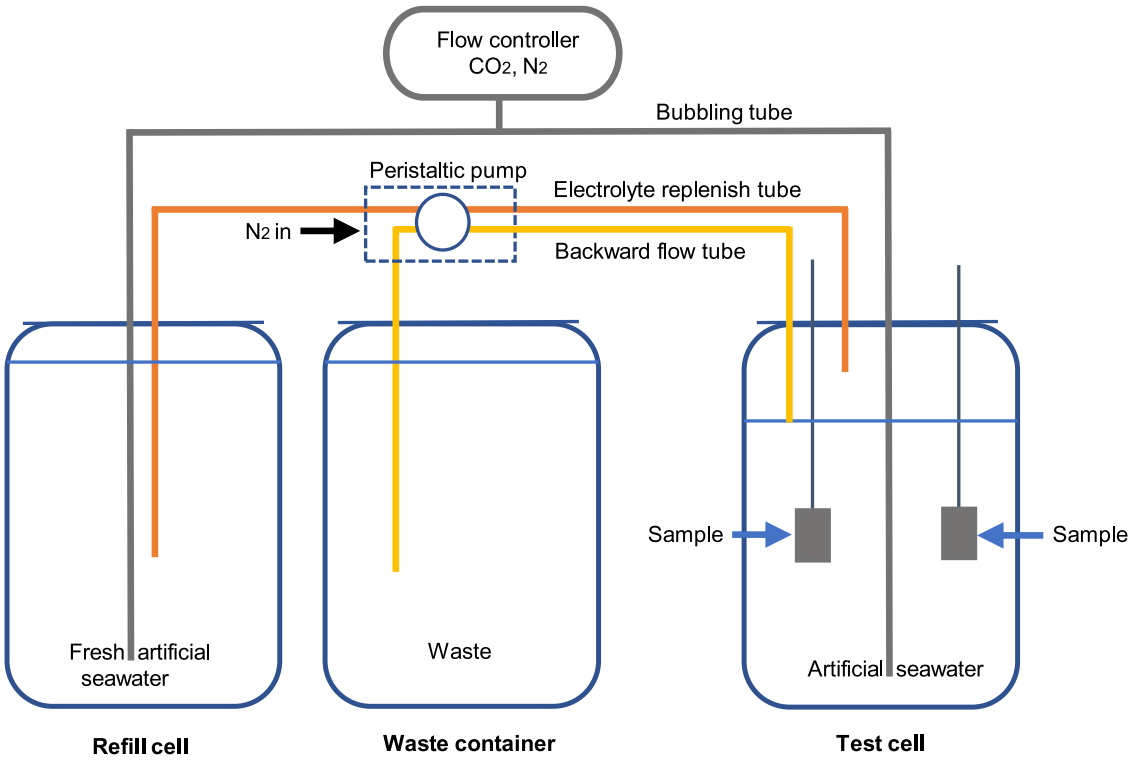

Fig. 1. Schematic of the corrosion test setup used for the CO_2 exposure. The test cell is replenished by fresh artificial seawater in CO_2 environment experiment, while in CO_2/H_2S environment experiment the precipitation of FeS kept the concentration of the dissolved Fe^{2+} ions low and therefore the test cell is not replenished by fresh artificial seawater.

Table 1
Chemical composition and the mechanical properties of the studied materials [18].

Material (wt%)	C	Al	Si	P	Mo	V	Cr	Mn	Ni	Cu	Hardness (HV_{10})	YS (MPa)	UTS (MPa)
$CS62$	0.62	0.26	0.40	0.23	0.46	0.70	0.61	1.36	0.89	0.75	386 ± 8	1100	1300
$CS65$	0.65	0.30	0.24	0.20	0.35	0.51	0.51	0.96	0.60	0.75	384 ± 6	1250	1400
$CS83$	0.83	0.19	0.35	0.30	0.35	0.54	0.55	1.07	0.69	0.59	453 ± 16	1400	1600

Table 2
Chemical composition of the corrosion test electrolyte [40].

Compound	NaCl	$MgCl_2$	Na_2SO_4	KCl	$NaHCO_3$	H_3BO_3	$SrCl_2$
Content (g/l)	24.53	5.2	4.09	0.695	0.201	0.027	0.025

2.3. Cathodic charging of hydrogen

An electrochemical charging using a 3.5% NaCl solution was used to introduce hydrogen in the materials at a constant potential of −1.4 V vs. Ag/AgCl reference electrode. 1 g/L thiourea was added to the solution as a poison to increase the efficiency of hydrogen absorption [42]. Materials were charged for the duration of their saturation limit based on their permeation diffusivity data [18]. In this regard, $CS62$, $CS65$, and $CS83$ were charged for 24, 192, and 168 h, respectively. To assure that they were fully saturated, another set of samples was charged for longer times than their calculated time for saturation limits. Hot extraction tests confirmed that all materials were fully saturated when they were charged for the duration of their saturation limit based on their permeation diffusivity data and no more hydrogen uptake is observed when they are charged longer. Besides, the charging condition was designed in a way to prevent any internal damage or blistering in the materials. After charging, samples were immediately immersed in liquid nitrogen.

This cathodic charging is done as a reference condition where no corrosion products are formed on the sample. This allows the reliable evaluation of the desorption activation energies linked to hydrogen trapping at microstructural constituents. The activation energy for H desorption is calculated using the simplified form of the Kissinger equation [43], which is proposed by Lee et al. [44]:

$$\frac{d(\ln \frac{\phi}{T_{max}^2})}{d(\frac{1}{T_{max}})} = -\frac{E_a}{R} \quad (1)$$

where ϕ is the heating rate (K min^{-1}), T_{max} (K) is the peak temperature, E_a (J K^{-1} mol^{-1}) is the hydrogen detrapping activation energy at T_{max}, and R (J K^{-1} mol^{-1}) is the universal gas constant.

2.4. Thermal desorption spectroscopy (TDS)

The TDS analysis was applied to measure the hydrogen concentration and analyze the hydrogen trapping in the charged samples mentioned in Sections 2.2 and 2.3 using the $G4-Phoenix$ analyzer. TDS analysis is based on the fundamental fact that hydrogen diffuses out from different microstructural features upon heating. Indeed, hydrogen desorbs at different temperatures from each microstructural feature depending on the corresponding binding energy [45]. The detected hydrogen concentration was quantified using the mass spectroscopy (MS) technique with a detection limit of 0.05 ppm(wt).

The hydrogen-charged samples, after corrosion testing (cf. Section 2.2) and after cathodic charging (cf. Section 2.3), were taken from the liquid nitrogen and washed in distilled water and acetone and dried fast (in less than one minute) before they were put into the quartz furnace. The hydrogen concentration was first measured by hot extraction

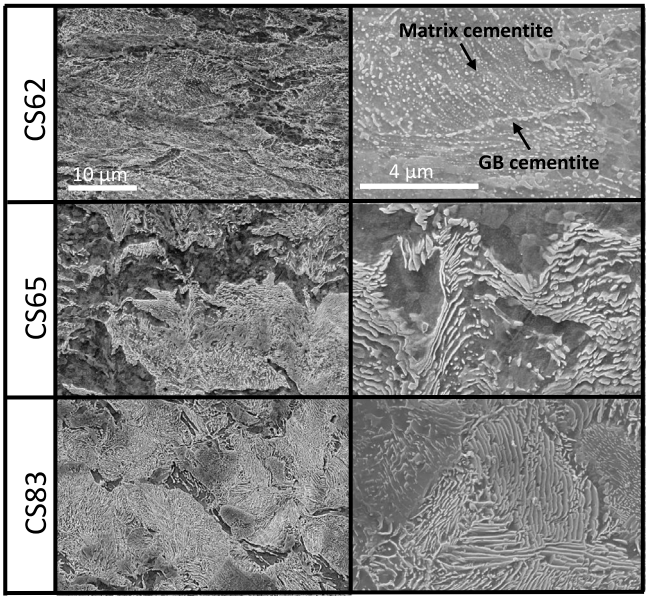

Fig. 2. SEM micrographs of the studied materials. The right column shows the higher magnification images of the materials' microstructure. The magnification of the SEM images in each column is the same for all materials.

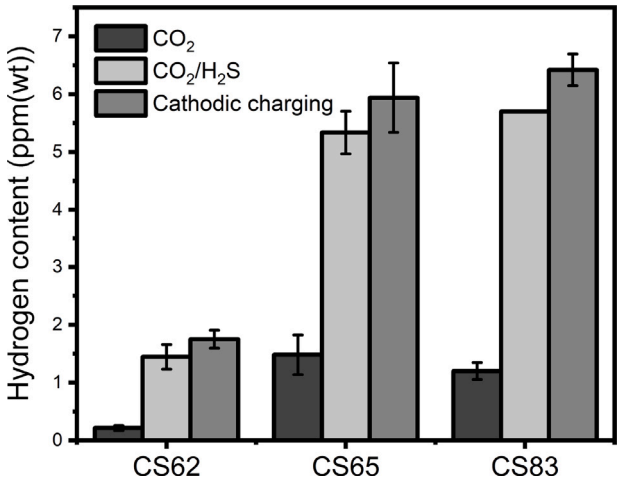

Fig. 3. Hydrogen content obtained by hot extraction at 650 °C for samples exposed to CO_2 and CO_2/H_2S environments for 21 days at room temperature and also after electrochemical charging to saturation. The columns show the mean value of three tests and the bars represent the standard deviation of the mean value. (The hot extraction tests which were done on two $CS83$ samples exposed to CO_2/H_2S environment were failed due to some technical errors of the machine. Therefore the data shown in this graph for material $CS83$ is not an average value).

method where the sample was inserted into the furnace which was pre-heated to 650 °C, an isothermal treatment to determine the hydrogen uptake level. In addition, the hydrogen trapping activation energies were analyzed (Eq. (1)) by heating the sample to 650 °C gradually, using three different heating rates, i.e., 0.2, 0.3, and 0.5 K/s. Three samples of each material and each environmental condition were tested by both hot extraction and TDS to ensure the reproducibility of the experiments.

3. Results

3.1. Microstructure characterization

The SEM results are presented in Fig. 2. The ferrite, cementite, and pearlite phase fractions for all materials, determined from the SEM micrographs analysis with ImageJ [46], are provided in Table 3. $CS62$ has a spheroidite microstructure with small grains of ferrite. The cementite morphology in $CS62$ is spherical or broken lamellae in a ferrite matrix. The cementite particles are located inside the ferrite grains (matrix cementite) and in the grain boundaries (GB cementite) as shown in Fig. 2 ($CS62$). $CS65$ shows a pearlite microstructure with thick lamellae of cementite in a ferrite matrix (Fig. 2 ($CS65$)). It should be noted that the ferrite grain size in $CS65$ is bigger and more connected in comparison with $CS62$. A predominantly lamellar pearlite microstructure with a lower fraction of ferrite in comparison with the other materials constitutes the microstructure of $CS83$.

3.2. Hot extraction

The hot extraction tests were done at 650 °C to determine total H uptake, including reversible, irreversible, and trapped H for $CS62$, $CS65$, and $CS83$ under the three exposure conditions. The results presented in Fig. 3 show that the hydrogen content in the samples which were cathodically charged to saturation for all materials is higher compared to the ones charged in CO_2 and CO_2/H_2S environments. The hydrogen contents in samples exposed to CO_2/H_2S environment remarkably increased in comparison with the samples charged in CO_2 environment. $CS62$ with a spheroidite microstructure shows a significantly lower amount of hydrogen uptake in all environments in comparison with $CS65$ and $CS83$ with ferrite/pearlite microstructure, while the carbon content in $CS62$ is quite close to $CS65$.

Table 3
Microstructures phase fraction and interlamellar spacing.

Material	Ferrite%	Cementite%	Pearlite%	Interlamellar spacing (nm)
$CS62$	91	9	81	–
$CS65$	90	10	85	242 ± 64
$CS83$	88	12	98	117 ± 30

3.3. Thermal desorption spectroscopy

3.3.1. CO_2 and CO_2/H_2S environment

Fig. 4 presents the TDS curves for $CS62$, $CS65$ and $CS83$ obtained at a heating rate of 0.5 K/s after exposure to the CO_2 and CO_2/H_2S environments for 21 days. The curves were fitted and deconvoluted into Gaussian curves with three, five, and four peaks for $CS62$, $CS65$, and $CS83$, respectively, in both environments. The shape of the TDS spectrum for each material differs significantly in these two environments. In addition, the highest temperature where H is detectable by TDS is higher for the materials corroded in CO_2 environment compared to CO_2/H_2S. The hydrogen uptake in $CS62$ in CO_2 environment is remarkably lower than the other materials and is very close to the detection limit of the $G4-Phoenix$ analyzer. Therefore the resultant curve is noisy and the shoulders in the curve are not necessarily representative of a peak. Due to this obscurity, the curve is not deconvoluted.

3.3.2. Cathodic charging

To investigate the role of corrosion layers formed during the exposure to CO_2 and CO_2/H_2S environments on the hydrogen desorption, the studied materials were cathodically charged with H in a 3.5% NaCl solution containing 1 g/L thiourea for TDS measurement. During electrochemical charging, no corrosion product formed on the surface of the materials, and the effect of the corrosion layers on H effusion was eliminated. As mentioned before, according to calculations, the saturation level was reached after 24, 192, and 168 h for $CS62$, $CS65$, and $CS83$, respectively [18]. The results of the TDS measurements obtained at a heating rate of 0.5 K/s are presented in Fig. 5.

It should be noted that H mobility within the body-centered cubic (BCC) materials is high [47–49]. The diffusion barrier between the tetrahedral sites in a BCC iron is 0.1 eV [48]. This fact implies that H starts to effuse from the samples immediately after the sample is taken out from the charging cell and before the start of the H measurement

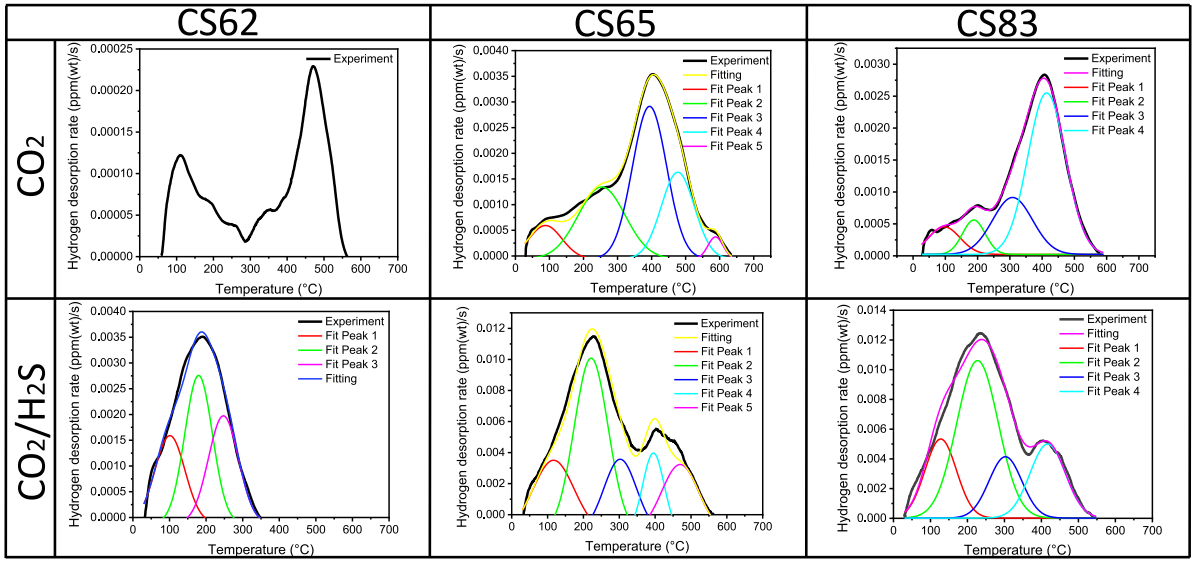

Fig. 4. *TDS* spectra obtained at a heating rate of 0.5 K/s for the studied materials exposed to 0.2 bar CO_2 and 0.2 bar CO_2/1 mbar H_2S environments for 21 days at room temperature. The deconvoluted curves is associated with the H desorption from particular microstructural features. (For interpretation of the references to color in this figure legend, the reader is referred to the web version of this article.)

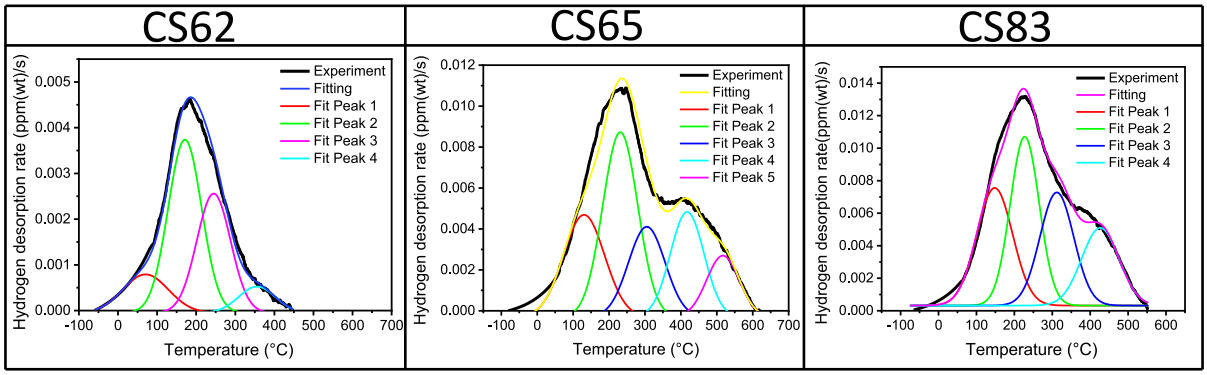

Fig. 5. *TDS* spectra obtained at a heating rate of 0.5 k/s for the studied materials charged cathodically with H till saturation. The deconvoluted curves are associated with the H desorption from particular microstructural features.

[50]. Pinson et al. [51] presented a numerical extrapolation towards cryogenic temperatures to compensate for the amount of H which is lost before the start of the *TDS* measurement. The *TDS* spectra shown in Fig. 5 are extrapolated towards cryogenic temperatures based on the method presented in [51]. A difference between the initial parts of the *TDS* spectrum is obvious when comparing the curves in Figs. 4 and 5. The initial sharp increase in the H effusion which is visible in the *TDS* spectrum in Fig. 4, has been replaced by a gradual increase in Fig. 5 using the numerical extrapolation towards cryogenic temperatures. Therefore, the H effusion starts from the negative temperatures in the *TDS* spectra in Fig. 5. This numerical extrapolation facilitates the *TDS* spectrum deconvolution. This allows a reliable determination of the desorption activation energies related to hydrogen trapping at specific microstructural features. Therefore, the cathodically charged samples, as a reference, are used for this purpose.

Fig. 5 illustrates that the *TDS* spectrum of *CS*62 is fitted with four peaks while it is fitted with three peaks under CO_2/H_2S environment (Fig. 4). The other two materials' *TDS* spectrum were deconvoluted to the same number of peaks as in CO_2 and CO_2/H_2S environments. The H desorption continues at higher temperatures for *CS*62 and *CS*65 which are charged cathodically in comparison with the same materials exposed to CO_2/H_2S environment (*cf*. Figs. 4 and 5). However, H desorption in *CS*83 shows the same ending temperature (around 550 °C) in both the CO_2/H_2S environment and under cathodic charging.

3.4. Peak analysis

The percentage of the total H content related to each deconvoluted peak is shown in Tables 4, 5 and 6 for CO_2 environment, CO_2/H_2S environment and the cathodic charging condition where possible, respectively. The activation energy of each peak was only calculated for the materials which were charged cathodically (Table 6). In CO_2 and CO_2/H_2S environments, the corrosion layer formed on the sample surface can affect both the absorption and desorption of hydrogen. Therefore, to calculate the trap energies of microstructural features, the cathodically charged samples were used.

4. Discussion

4.1. Effect of charging conditions on hydrogen uptake

The studied materials were submitted to three different charging conditions, 0.2 bar CO_2 environment, 0.2 bar CO_2/1 mbar H_2S environment, and cathodic charging using 1 g/L thiourea in a 3.5% NaCl solution. To investigate the hydrogen uptake in a CO_2 environment, one should consider that CO_2 has a significant contribution to the corrosion of carbon steel and corrosion plays an important role in the hydrogen generation and absorption. The higher cathodic currents in the presence of CO_2 in aqueous solutions due to the H_2CO_3 buffering effect [52]

Table 4
The data obtained from the peak analysis of TDS results of the samples exposed to the CO_2 environment.

Peak	*CS*62		*CS*65		*CS*83	
	T_{max} (°C)	H fraction (%)	T_{max} (°C)	H fraction (%)	T_{max} (°C)	H fraction (%)
1st peak	–	–	89 ± 6	7	93 ± 7	8.4
2nd peak	–	–	250 ± 3	26.1	184 ± 6	8.2
3rd peak	–	–	386 ± 10	42.4	303 ± 6	23.2
4th peak	–	–	471 ± 6	22.5	409 ± 7	60.2
5th peak	–		584 ± 9	2	–	–

Table 5
The data obtained from the peak analysis of TDS results of the samples exposed to the CO_2/H_2S environment.

Peak	*CS*62		*CS*65		*CS*83	
	T_{max} (°C)	H fraction (%)	T_{max} (°C)	H fraction (%)	T_{max} (°C)	H fraction (%)
1st peak	100 ± 2	25.3	110 ± 9	17	131 ± 5	18
2nd peak	176 ± 5	42.5	183 ± 9	44.8	224 ± 5	48
3rd peak	244 ± 4	32.2	296 ± 6	13.9	303 ± 6	15
4th peak	–	–	387 ± 12	10.3	403 ± 9	19
5th peak	–	–	462 ± 11	14	–	–

Table 6
The data obtained from the peak analysis of TDS results of the samples charged under the cathodic charging condition.

Peak	*CS*62			*CS*65			*CS*83		
	T_{max} (°C)	H fraction (%)	Activation energy (kJ/mol)	T_{max} (°C)	H fraction (%)	Activation energy (kJ/mol)	T_{max} (°C)	H fraction (%)	Activation energy (kJ/mol)
1st peak	80 ± 9	12	15.2	141 ± 10	21.4	14.3	154 ± 17	27.2	18.6
2nd peak	164 ± 7	48	15	228 ± 10	34.6	17.1	227 ± 5	28.6	37.8
3rd peak	251 ± 7	33	26.4	314 ± 11	16.6	19.9	313 ± 17	25	35
4th peak	349 ± 7	7	63.8	423 ± 8	18.1	35.3	415 ± 12	19.2	64
5th peak	–	–	–	514 ± 9	9.3	69.3	–	–	–

and the reduction of H_2CO_3 and HCO_3^- close to the surface is vastly reported in previous studies [53–55]. This results in an increased H^+ availability on the carbon steel surface according to the following reactions [54,56]:

$$CO_2 + H_2O \rightleftarrows H_2CO_3 \quad (2)$$

$$H_2CO_3 \rightleftarrows H^+ + HCO_3^- \quad (3)$$

$$HCO_3^- \rightleftarrows H^+ + CO_3^{2-} \quad (4)$$

The generated H^+ ions in the above-mentioned reactions can adsorb on the metal surface through the Volmer reaction (Eq. (5)) and combine to form H_2 molecules through the Tafel chemical reaction (Eq. (6)) [57]:

$$H^+ + e^- \rightleftarrows H_{(ads)} \quad (5)$$

$$H_{(ads)} + H_{(ads)} \rightleftarrows H_2 \quad (6)$$

Or through the electrochemical Heyrovsky reaction [58]:

$$H_{(ads)} + H^+ + e^- \rightleftarrows H_2 \quad (7)$$

Or they can absorb to the subsurface and then diffuse into the steel [59]:

$$H_{(ads)} \rightleftarrows H_{(abs)} \quad (8)$$

In a CO_2/H_2S coexisting environment, the corrosion behavior is more vague and intricate and even a small amount of CO_2 in an H_2S environment or a small amount of H_2S in a CO_2 environment can affect the corrosion significantly compared to the pure H_2S or CO_2 environments, respectively. As it is discussed above, CO_2 can react with water and form acid and then decompose and generate a proton (Eqs. (2)–(4)). H_2S can also decompose to HS^- and S^{2-} and generate protons [60,61]:

$$H_2S \rightleftarrows H^+ + HS^- \quad (9)$$

$$HS^- \rightleftarrows H^+ + S^{2-} \quad (10)$$

In a CO_2/H_2S mixed environment, the amount of H which is available on the steel surface is higher compared to pure CO_2 environment due to the synergistic effects of CO_2 and H_2S on corrosion and H generation. The hydrogen uptake in all studied materials shows a higher value in CO_2/H_2S environment compared with the results in pure CO_2 environment as shown in Fig. 3. The significant difference between the hydrogen uptake in these two environments can be correlated to the fact that in CO_2 environment, the dissociation and H generation process includes one more step which is related to the dissolution of CO_2 in water and forming carbolic acid (Eq. (2)), while the direct dissociation process of H_2S (Eq. (9)) in CO_2/H_2S environment accelerates the H generation. Besides, in environments containing sulfur species, the kinetics of the evolution of gaseous hydrogen or the recombination of atomic H (Eqs. (6) and (7)) is slowed down significantly. Therefore, the adsorption of atomic H on the material surface increases [62–64].

During cathodic charging, the cathodic reaction rate is increased and generates more H atoms and at the same time enhances the H atom recombination rate (Eqs. (6) and (7)) [59]. In this study, however, thiourea is added to the cathodic charging electrolyte to decrease the H recombination rate and increase the amount of absorbed H into the material. Therefore as it can be seen in Fig. 3, the H uptake is higher for all the materials which are cathodically charged in comparison with the materials corroded in CO_2 and CO_2/H_2S environments.

*CS*65 and *CS*83 display two distinct peaks before deconvolution in CO_2/H_2S environment which are shown by black color in Fig. 4. One peak at a lower temperature originates from reversible hydrogen and one at a higher temperature originates from deep-trapped hydrogen. In cathodic charging, these two peaks are closer to each other in both materials (Fig. 5). Kirchheim [65] discussed that when these two peaks are separated sufficiently, the deep trap sites stay filled during the first peak hydrogen desorption. At higher temperatures, when the second peak is revealed, the hydrogen from the deep traps starts to effuse out of the sample. The saturation after cathodic charging

causes the overlap between the peaks of hydrogen desorption from the different traps. Indeed after saturation, the diffusible hydrogen traps like grain boundaries and dislocations are filled with hydrogen and the hydrogen desorption from these traps continues even at higher temperatures. Therefore, the hydrogen desorption from the diffusible traps can overlap with high-temperature peaks.

Although the same trap density is available in each microstructure, the trap occupancy differs depending on the environment and equilibrium obtained (depending on the total hydrogen uptake). In the corrosion exposure testing (CO_2 and CO_2/H_2S environments), the occupancy of the reversible trap sites was lower due to the lower uptake level, while a higher concentration was obtained for the cathodically charged exposure. This affects the equilibrium between the lower and higher trapping sites in the microstructure, which can result in the observed variations in the overlapping of the different peaks. Nevertheless, since the corrosion layers can also affect desorption, the most reliable interpretation of trap sites can only be done based on the cathodically charged samples.

4.2. Effect of microstructure on hydrogen uptake

When H penetrates a material, it interacts with the microstructural defects and sometimes it is trapped in a defect to decrease its energy. The results in Fig. 3 confirm that in CO_2/H_2S environment and cathodic H charging condition, the H uptake increases with carbon content and $CS83$ exhibits the highest amount of H uptake. There is a significant difference between H uptake in $CS62$ and $CS65$. The carbon content of these two materials is very close (0.62% and 0.65%). However, the $CS62$ microstructure consists of the spherical or broken lamella of cementite in a ferrite matrix while $CS65$ shows a pearlite/ferrite microstructure with thick lamellae of cementite in a ferrite matrix (Fig. 2). The significant difference between the H uptake of these two materials shows that the microstructure and the morphology and distribution of the cementite phase play a more important role than the carbon content in the H uptake capacity in carbon steels. Amemiya et al. [66] showed in their Electron Backscatter Diffraction ($EBSD$) analysis that the lattice parameters ratios of the cementite lamellae are completely different from the spheroidized cementite particles which indicates that a lamellar pearlite microstructure has a certain amount of internal stress. The internal stress in a lamellar microstructure can cause a higher H uptake in $CS65$ in comparison with $CS62$. Moreover, the cementite/ferrite interface area in a lamellar microstructure of $CS65$ is higher than this area in a spheroidite microstructure of $CS62$.

The H uptake in $CS83$ is slightly higher than that in $CS65$ in both CO_2/H_2S environment and under cathodic charging. The high amount of cementite/ferrite interfaces in $CS83$ leads to a higher H uptake in comparison with $CS65$. Furthermore, since the grain size and the pearlite colony size in $CS83$ are finer than in $CS65$ [18], this material has more area of pearlite/pearlite interfaces in its microstructure. The high susceptibility of pearlite/pearlite interfaces to H embrittlement has previously been investigated and published by the present authors [39]. Therefore $CS83$ shows a higher capacity for H uptake.

According to the deconvoluted peaks in Fig. 5 which are related to the cathodic charging condition, the first three peaks show very similar activation energies for all materials, in a range of 15 to 37.8 kJ/mol (Table 6). Correlating each peak with the particular microstructural defects would not be straightforward. However, using the activation energies found in the literature one can relate these peaks to the microstructural defects with a reasonable approximation. For instance, the activation energy for hydrogen desorption in different microstructural defects based on the literature are as follows: 0–20 kJ/mol for elastic strain field of dislocations [67], 17–60 kJ/mol for screw dislocation cores and grain boundaries [68–70], 30–50 kJ/mol for micro-voids, voids and vacancies [67,71], and 41–59 kJ/mol for cementite vacancies [72]. In a pearlitic microstructure, the hydrogen trapping activation energy within the ferrite/cementite interfaces is reported in a wide range from 10.85 to 66.3 kJ/mol [72–76]. Some studies considered the ferrite/cementite interface as a reversible trap [77] while others correspond it to the irreversible hydrogen trapping sites [75,76]. With a comparison between the activation energies reported in the literature and the calculated activation energies in Table 6, the first three deconvoluted peaks in all the materials can be related to grain boundaries, dislocations, micro-voids, and vacancies.

Based on Table 6 for cathodic charging the diffusible hydrogen fraction (sum of the first three peaks) in $CS62$ is 93% which is higher than for $CS83$ (≅81%). It should be noted that this comparison is between the hydrogen fraction relative to the total hydrogen in both materials and it is obvious from Fig. 5 that the diffusible peaks (1,2 and 3) in $CS83$ contain more hydrogen in comparison with the same peaks in $CS62$. In $CS62$, the spherical or broken lamella of cementite particles is dispersed in the ferrite grains. In $CS83$ cementite lamellar morphology constitutes the pearlitic microstructure. Therefore, the boundaries between the prior-austenite grains are the boundaries between two ferritic grains in $CS62$, while in $CS83$, they are the boundaries between two pearlite colonies. As discussed before, the pearlite/ferrite and the pearlite/pearlite boundaries are incoherent and high-energy interfaces that are susceptible to hydrogen embrittlement. The stress field due to the volume change during the austenite to pearlite transformation, exposes a high tension in these interfaces with high dislocation density [19]. These boundaries are a suitable trap for hydrogen accumulation [39]. The fourth deconvoluted peak in $CS83$ is related to the presence of a large area of pearlite/pearlite interfaces, while in $CS62$, there is not any high-temperature peak in CO_2/H_2S environment. In this material, only after cathodic charging and saturation, the high-temperature peak (fourth peak) appears (Fig. 5 and Table 6). In fact, in $CS62$ the interfaces between the prior-austenite grains are not of the same type as in $CS83$. As mentioned before, these interfaces are the boundaries between two ferrite grains which are not considered as irreversible traps as the pearlite/pearlite or pearlite/ferrite interfaces in $CS65$ and $CS83$. Therefore, the diffusible hydrogen fraction related to ferrite/cementite interfaces, dislocations, vacancies, and grain boundaries in $CS62$ is higher than for the two other materials.

The sum of the H fraction of peaks 1, 2, and 3 is almost the same in CO_2/H_2S environment and cathodic charging for $CS65$ and $CS83$ (H fraction related to peak 1,2 and 3 for $CS65$ is 75.7% and 72.6% in CO_2/H_2S environment and cathodic H charging condition, respectively, while for $CS83$ is ≅81% in both CO_2/H_2S environment and cathodic H charging condition). This means that the reversible peaks (peaks 1, 2, and 3) are filled with almost the same amount of H in both charging conditions. The H fugacity is high enough in both CO_2/H_2S and cathodic charging conditions to fill the reversible traps. In $CS65$, this H fraction is higher in CO_2/H_2S environment (75.7%) in comparison with the cathodic charging condition (72.6%) whose reason is explained in the next paragraph. For $CS62$, in CO_2/H_2S environment, all three peaks are considered to be related to the reversible H, while under cathodic charging a small irreversible H peak appears with the H fraction of 7%.

To analyze the irreversible peaks, it should first be noted that as shown in Figs. 4 and 5, the TDS spectrum of $CS65$ deconvoluted to 5 peaks, i.e that this material exhibits two irreversible peaks while $CS83$ shows one irreversible peak. These two materials exhibit a lamellar cementite morphology. The fourth peak in the TDS spectrum of $CS65$ with the maximum temperature of 423 ± 8 °C (Table 6) can be correlated to the release of H from the previous reversible trap with the maximum temperature of 314 ± 11 °C. The activation energy of the fourth peak of $CS65$ is 35.3 kJ/mol which is similar to the activation energy of peak 3 in $CS83$ that has almost the same maximum temperature of the third peak in $CS65$ as is shown in Table 6 (314 ± 11 °C and 313 ± 17 °C, respectively). Therefore, the fourth peak in $CS65$ can be a part of the third peak in this material whose H desorbs with a delay. Based on electrochemical permeation tests done by Skilbred et al. [18] on the

same materials as this study, $CS65$ showed the highest time lag and the lowest diffusion coefficient. Furthermore, $CS65$ has the highest amount of tortuosity [18]. All of the above-mentioned parameters delay the H desorption from the traps. This can explain the higher temperature in which the H desorption stops in $CS65$ compared to the other materials as well (Fig. 5). As a result, it seems reasonable to verify the idea that the fourth peak is a part of the third peak which desorbs with a delay. This observation is in agreement with Takai et al. [75] who showed that the high-temperature peak in the TDS spectrum consists of non-diffusible hydrogen and a part of diffusible hydrogen in high-strength steel. The fifth peak in $CS65$ can correspond to the fourth peak of $CS62$ and $CS83$ whose activation energies are close to each other (69.3, 63.8 and 64 kJ/mol, respectively (Table 6)). The H fraction related to each trap in Table 6 shows that the fourth peak in $CS83$ contains ≅19.2% of the total H, while the H fraction in the corresponding peaks in $CS62$ and $CS65$ are 7% (fourth peak) and 9.3% (fifth peak), respectively. These irreversible peaks are related to the pearlite/pearlite and/or pearlite/ferrite interfaces which are strong traps for H. As discussed previously, $CS83$ has the highest amount of pearlite/pearlite interfaces, therefore this interface-related peak contains the highest amount of H fraction in this material compared to the other materials.

With a comparison between Fig. 4 (CO_2/H_2S environment) and Fig. 5, the temperatures at which the H desorption stops are higher in values in cathodic charging conditions for $CS62$ and $CS65$. After cathodic charging, more irreversible trap sites are filled by H and cause the H to effuse out at a higher temperature as it can be seen in the TDS spectrum of $CS62$ and $CS65$ compared to the same materials in CO_2/H_2S environment. The H desorption from the deeper traps (peaks 3 and 4 in $CS62$ and peaks 4 and 5 in $CS65$) retards to higher temperatures after cathodic charging (Figs. 4 and 5, Tables 5 and 6). Since the grain size or the pearlite colony size is smaller in $CS83$ and therefore more pearlite/pearlite or pearlite/ferrite interfaces exist in its microstructure, it was expected that the same trend is observed for $CS83$. Moreover, the activation energies of the peaks are almost the same in all materials. However, in $CS83$ the H desorption stops at the same temperature in both CO_2/H_2S environment and in cathodic H charging condition (Fig. 4 (CO_2/H_2S environment) and Fig. 5). As it is shown in Tables 5 and 6, for $CS83$ the H fraction related to the reversible peaks (Peaks 1, 2 and 3) is ≅81% and the H fraction related to the irreversible peak is ≅19.2% in both CO_2/H_2S environment and cathodic H charging condition. Therefore it can be inferred that due to the higher fugacity with cathodic charging, deep traps in $CS62$ and $CS65$ can be more activated while in $CS83$ a higher fugacity is not required to activate deep trap more efficiently.

4.3. Effect of corrosion layer on hydrogen desorption

In Fig. 4, the TDS spectra of all studied materials charged in CO_2 environment, displays that the diffusible or reversible H desorbs gradually leading to a peak related to the irreversible H desorption appearing. Since the H uptake for $CS62$ in CO_2 environment is close to the detection limit of the $G4-Phoenix$, its TDS spectrum is too noisy. Therefore, the TDS spectrum for $CS62$ in CO_2 environment is not deconvoluted. For $CS65$ and $CS83$, the deconvolution is done similarly as for the other conditions. $CS65$ and $CS83$ are deconvoluted to five and four peaks, respectively. However, based on Tables 4, 5 and 6, the reversible and irreversible H fraction is quite different than the same peaks from the same material in the CO_2/H_2S environment or cathodic H charging condition. If the first three peaks in $CS65$ and $CS83$ are considered as the reversible peaks which are related to the traps like ferrite/cementite interfaces, dislocations, micro-voids, and grain boundaries [68], the sum of the H fractions related to the first three peaks in $CS83$ is ≅81% and the H fraction related to the fourth peak which is the irreversible peak is ≅19.2% for both CO_2/H_2S environment and in cathodic H charging condition. For $CS83$, in CO_2 environment the reversible and irreversible H fractions are 39.8% and 60.2%, respectively which is quite different than the corresponding H fractions in CO_2/H_2S environment or cathodic H charging condition. A similar trend can be seen in $CS65$ as well. However, it should be noted that as discussed in the previous section, the fourth peak in this material has a complexity and it can be related to the H desorption from a reversible trap which appears with a delay. To investigate the difference between the TDS spectrum of the studied materials in CO_2 environment and CO_2/H_2S environment, the corrosion layer formed on the surfaces of the materials during the charging process should be studied.

Fig. 6 shows the cross sections of the corrosion layers formed on all materials in both CO_2 and CO_2/H_2S environment. Under cathodic H charging, no corrosion layer is formed. First of all the SEM images show a significant difference in the thickness of the corrosion layers formed on the materials in CO_2 and CO_2/H_2S environment. The corrosion layer thickness range is 17–25 μm for CO_2 environment while it is less than 1 μm for CO_2/H_2S environment. From the thickness observation, it can be deduced that H has to go through a longer route to effuse out from the materials exposed to CO_2 environment. In addition to the thickness, the morphology of the corrosion layer can have a determinant role in H desorption. In a ferritic-pearlitic microstructure, a micro-galvanic cell forms between the ferrite and cementite lamellae which act as the anode and cathode, respectively [78,79]. Therefore, the ferrite lamellae or grains dissolve while the cementite lamellae which are the cathodic components remain in the corrosion layer [80]. The remaining cementite layers in galvanic corrosion cause the corrosion layer to adopt almost the same morphology as the microstructure of the material as can be seen in Fig. 6 for $CS65$ and $CS83$. Therefore, H passes a tortuous path to effuse out of the materials exposed to CO_2 environment. Skilbred et al. [18] used the same materials as in this study in an electrochemical hydrogen permeation cell to measure the hydrogen permeation flux through the steels. Their results showed that the hydrogen uptakes reduced in the steels with the accumulation of remaining Fe_3C, despite increasing corrosion rates over time. They explained that in both pure CO_2 corrosion and in the presence of a small amount of H_2S (less than 1 mbar) hydrogen adsorbed on remaining Fe_3C which is located far from the ferrite phase on the surface of the material and therefore has a small chance for absorption into the steel since the hydrogen diffusivity and solubility in Fe_3C phase is low. In the present study during the TDS measurement both the hydrogen absorbed and uptaken by the material and the hydrogen trapped in the remaining Fe_3C in the corrosion layer is measured.

It can be inferred that in materials exposed to the CO_2 environment, H desorbs with a delay due to the fact that H passes through a tortuous corrosion layer containing remaining Fe_3C that is partially filled with corrosion products and can trap the hydrogen and release it with a delay and as a result the shape of the TDS spectrum is different in this condition (Fig. 4). H desorbs gradually at first due to the slow movement of H through the tortuous corrosion layer. Then a peak appears in higher temperatures which is related to the H desorption delay. In CO_2/H_2S environment, the fast formation of iron sulfide layer in the first stages of corrosion [81] decreases the corrosion rate significantly and therefore a thinner corrosion layer forms under this environmental condition. With a comparison between the TDS spectrum for materials after exposure to CO_2/H_2S environment (Fig. 4) and after cathodic charging (Fig. 5), it can be concluded that the thin corrosion layer formed in CO_2/H_2S environment layer does not change the H desorption rate. These results are in agreement with the study performed by Silva et al. [82]. They evaluated the susceptibility of $API\ 5L\ X65$ steel to hydrogen uptake and hydrogen embrittlement in CO_2 environment containing a low concentration of H_2S, at OCP. Their results displayed that FeS film formed on the steel surface has no effect on hydrogen uptake, but reduced the corrosion rate. Huang et al. [36] showed in their experiments that the iron sulfide film blocks the hydrogen permeation through the steel. However, their results displayed that the iron sulfide film which is formed in low concentration

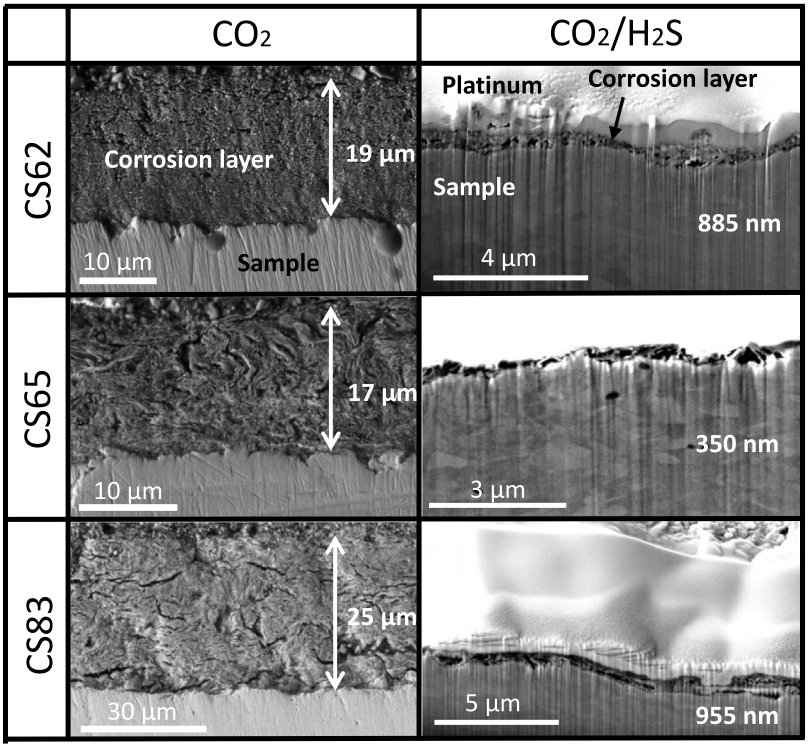

Fig. 6. Cross-section morphologies of the corrosion layers of the studied materials exposed to 0.2 bar CO_2 (left column) and 0.2 bar CO_2/1 mbar H_2S (right column) environments for 21 days. The surface of the samples, exposed to 0.2 bar CO_2/1 mbar H_2S environment, were covered with platinum before milling to protect the nano-scale corrosion layers. The numbers written in each image are the average thickness of the corrosion layers of two samples for each material and environment.

of H_2S has a small effect on hydrogen uptake. Another investigation by Kappes et al. [83] presented that the amount of H_2S is a crucial factor in the formation of the iron sulfide layer and its ability on reducing the hydrogen uptake. In this study, the H_2S concentration is 1 mbar which is considered low. Therefore, the corrosion layer that formed on the material, which is supposed to be a combination of Fe_3C, $FeCO_3$ and FeS, does not make a barrier to retard hydrogen uptake and hydrogen effusion.

5. Conclusions

Hydrogen thermal desorption and hot extraction analysis were performed on three high-strength carbon steels with different cementite morphology and microstructure. These materials were exposed to modified artificial seawater bubbled with CO_2 and H_2S at open circuit potential. The same materials were also charged cathodically in a 3.5% NaCl solution containing 1 g/L thiourea. TDS and hot extraction were performed on the materials after testing to evaluate the role of different environments and charging conditions, cementite morphology, and the corrosion layer on hydrogen uptake and hydrogen desorption. All tests were done at room temperature. The following conclusions can be drawn from the present study:

- The hydrogen uptake in all studied materials shows a higher value in the CO_2/H_2S environment compared with the results in the pure CO_2 environment. The H uptake is higher for all materials which are charged cathodically to their saturation in comparison with the materials exposed to CO_2 and CO_2/H_2S environments.
- In CO_2/H_2S environment and cathodic H charging condition, the H uptake increases with carbon content.
- The hydrogen uptake in the material with the lamellar cementite morphology is significantly higher than the material with the spherical cementite morphology with almost similar carbon content, in CO_2/H_2S environment, and cathodic H charging condition.
- In CO_2 environment, the H uptake and the hydrogen desorption are affected by the corrosion layer formed on the steel. In this condition, H desorbs with a delay because H passes through a tortuous corrosion layer containing remaining Fe_3C partially filled with corrosion products that can trap H and release it with a delay.
- The pearlite/ferrite and pearlite/pearlite interfaces act as strong irreversible traps in pearlitic microstructures.
- In CO_2/H_2S environment and cathodic H charging condition, the tortuosity in the lamellar pearlitic microstructures delays the H desorption from the traps. This leads to H desorption continuing at higher temperatures. The high-temperature peak in the TDS spectrum of the lamellar pearlitic microstructures can consist of non-diffusible hydrogen and a part of diffusible hydrogen.
- The thin corrosion layer forms in CO_2/H_2S environment does not affect the H desorption rate while based on our previous study it retards the corrosion rate.

CRediT authorship contribution statement

Shabnam Karimi: Conceptualization, Data curation, Investigation, Methodology, Visualization, Writing – original draft, Writing – review & editing. **Iman Taji:** Conceptualization, Data curation, Investigation, Methodology, Writing – review & editing. **Simona Palencsár:** Conceptualization, Data curation, Investigation, Methodology, Writing – review & editing. **Arne Dugstad:** Conceptualization, Data curation, Investigation, Methodology, Writing – review & editing. **Tarlan Hajilou:** Methodology, Writing – review & editing. **Afrooz Barnoush:** Funding acquisition, Supervision, Writing – review & editing. **Kim Verbeken:** Supervision, Writing – review & editing. **Roy Johnsen:** Conceptualization, Funding acquisition, Supervision, Writing – review & editing. **Tom Depover:** Supervision, Writing – review & editing.

Declaration of competing interest

The authors declare the following financial interests/personal relationships which may be considered as potential competing interests: Shabnam Karimi reports financial support was provided by Norwegian University of Science and Technology.

Data availability

Data will be made available on request

Acknowledgments

This work was performed as part of the KPN project "Environmental Cracking of Flexible Pipe Armour Wires", Research Council of Norway project no. 280760 within the $PETROMAKS$ 2 program. The authors would like to thank the following project participants for financial and technical support: The Research Council of Norway, Norway; Equinor, Norway; Shell, Norway; Chevron, United States of America; Petrobras, Brazil; OKEA, Norway; TechnipFMC, France; NOV, Denmark; Baker Hughes, United Kingdom; 4Subsea, Norway.

References

[1] X. Li, M.A. Vaz, Analytical estimation on the number of bending cycles to initiate armour wires lateral buckling in flexible pipes, Ocean Eng. 228 (2021) 108838.
[2] M. Tang, S. Li, H. Zhang, X. Bian, X. Zhao, Monitoring the slip of helical wires in a flexible riser under combined tension and bending, Ocean Eng. 256 (2022) 111512.
[3] S. Papavinasam, Corrosion Control in the Oil and Gas Industry, Elsevier, 2013.
[4] G. Zhang, Y. Cheng, Localized corrosion of carbon steel in a CO_2-saturated oilfield formation water, Electrochim. Acta 56 (3) (2011) 1676–1685.
[5] G. Cooney, J. Littlefield, J. Marriott, T.J. Skone, Evaluating the climate benefits of CO_2-enhanced oil recovery using life cycle analysis, Environ. Sci. Technol. 49 (12) (2015) 7491–7500.
[6] S.C. da Silva, E.A. de Souza, F. Pessu, Y. Hua, R. Barker, A. Neville, J.A.d.C.P. Gomes, Cracking mechanism in API 5L X65 steel in a CO_2-saturated environment, Eng. Fail. Anal. 99 (2019) 273–291.
[7] S.Y. Kondrat'ev, A. Al'khimenko, A. Khar'kov, O. Shvetsov, A. Davydov, Criteria for accelerated estimation of susceptibility of pipe steels to corrosion cracking under oilfield conditions, Metal Sci. Heat Treat. 63 (9) (2022) 533–539.
[8] O. Zvirko, O. Tsyrulnyk, N. Kret, Susceptibility of steel sucker rods operated in oil well to environmentally assisted fatigue, in: Fatigue and Fracture of Materials and Structures, Springer, 2022, pp. 119–125.
[9] X. Wen, P. Bai, B. Luo, S. Zheng, C. Chen, Review of recent progress in the study of corrosion products of steels in a hydrogen sulphide environment, Corros. Sci. 139 (2018) 124–140.
[10] L. Li, J. Wang, J. Xiao, J. Yan, H. Fan, L. Sun, L. Xue, Z. Tang, Time-dependent corrosion behavior of electroless Ni–P coating in H2S/Cl- environment, Int. J. Hydrogen Energy 46 (21) (2021) 11849–11864.
[11] Y. Baik, Y. Choi, The effects of crystallographic texture and hydrogen on sulfide stress corrosion cracking behavior of a steel using slow strain rate test method, Phys. Metals Metallogr. 115 (13) (2014) 1318–1325.
[12] M. Mohtadi-Bonab, M. Eskandari, K. Rahman, R. Ouellet, J. Szpunar, An extensive study of hydrogen-induced cracking susceptibility in an API X60 sour service pipeline steel, Int. J. Hydrogen Energy 41 (7) (2016) 4185–4197.
[13] M. Mohtadi-Bonab, J. Szpunar, R. Basu, M. Eskandari, The mechanism of failure by hydrogen induced cracking in an acidic environment for API 5L X70 pipeline steel, Int. J. Hydrogen Energy 40 (2) (2015) 1096–1107.
[14] C. Dong, Z. Liu, X. Li, Y. Cheng, Effects of hydrogen-charging on the susceptibility of X100 pipeline steel to hydrogen-induced cracking, Int. J. Hydrogen Energy 34 (24) (2009) 9879–9884.
[15] Z. Liu, X. Gao, L. Du, J. Li, P. Li, C. Yu, R. Misra, Y. Wang, Comparison of corrosion behaviour of low-alloy pipeline steel exposed to H_2S/CO_2-saturated brine and vapour-saturated H_2S/CO_2 environments, Electrochim. Acta 232 (2017) 528–541.
[16] P. Kedzierzawski, Hydrogen trapping in iron and iron alloys, in: Hydrogen Degradation of Ferrous Alloys, Noyes Publications, 1985, pp. 271–288.
[17] T. Depover, K. Verbeken, The detrimental effect of hydrogen at dislocations on the hydrogen embrittlement susceptibility of Fe-CX alloys: An experimental proof of the HELP mechanism, Int. J. Hydrogen Energy 43 (5) (2018) 3050–3061.
[18] E.S. Skilbred, M. Kappes, M. Iannuzzi, R. Johnsen, Hydrogen uptake and diffusivity in steel armor wires with different chemical composition, carbide distribution, grain size, and degree of deformation, Mater. Corros. 73 (3) (2022) 326–345.
[19] S. Chan, J. Charles, Effect of carbon content on hydrogen occlusivity and embrittlement of ferrite–pearlite steels, Mater. Sci. Technol. 2 (9) (1986) 956–962.
[20] X. Zhu, W. Li, H. Zhao, L. Wang, X. Jin, Hydrogen trapping sites and hydrogen-induced cracking in high strength quenching & partitioning (Q&P) treated steel, Int. J. Hydrogen Energy 39 (24) (2014) 13031–13040.
[21] M.M. Islam, C. Zou, A.C. Van Duin, S. Raman, Interactions of hydrogen with the iron and iron carbide interfaces: a ReaxFF molecular dynamics study, Phys. Chem. Chem. Phys. 18 (2) (2016) 761–771.
[22] D. Staicopolus, The role of cementite in the acidic corrosion of steel, J. Electrochem. Soc. 110 (11) (1963) 1121.
[23] F. Farelas, M. Galicia, B. Brown, S. Nesic, H. Castaneda, Evolution of dissolution processes at the interface of carbon steel corroding in a CO_2 environment studied by EIS, Corros. Sci. 52 (2) (2010) 509–517.
[24] A. Dugstad, Mechanism of protective film formation during CO_2 corrosion of carbon steel, in: CORROSION 98, OnePetro, 1998.
[25] D. Lopez, W.d. Schreiner, S. De Sánchez, S. Simison, The influence of carbon steel microstructure on corrosion layers: an XPS and SEM characterization, Appl. Surf. Sci. 207 (1–4) (2003) 69–85.
[26] J. Crolet, N. Thevenot, S. Nesic, Role of conductive corrosion products in the protectiveness of corrosion layers, Corrosion 54 (3) (1998) 194–203.
[27] W. Hui, Z. Xu, Y. Zhang, X. Zhao, C. Shao, Y. Weng, Hydrogen embrittlement behavior of high strength rail steels: A comparison between pearlitic and bainitic microstructures, Mater. Sci. Eng. A 704 (2017) 199–206.
[28] Y. Ogawa, H. Nishida, M. Nakamura, V. Olden, A. Vinogradov, H. Matsunaga, Dual roles of pearlite microstructure to interfere/facilitate gaseous hydrogen-assisted fatigue crack growth in plain carbon steels, Int. J. Fatigue 154 (2022) 106561.
[29] R.d.C.P. Loureiro, M. Beres, M. Masoumi, H.F.G. de Abreu, The effect of pearlite morphology and crystallographic texture on environmentally assisted cracking failure, Eng. Fail. Anal. 126 (2021) 105450.
[30] A. Bott, D. Dos Santos, P. De Miranda, Influence of cementite morphology on the hydrogen permeation parameters of low-carbon steel, J. Mater. Sci. Lett. 12 (6) (1993) 390–393.
[31] V. Ramunni, T.D.P. Coelho, P.V. de Miranda, Interaction of hydrogen with the microstructure of low-carbon steel, Mater. Sci. Eng. A 435 (2006) 504–514.
[32] P. Bai, Y. Liang, S. Zheng, C. Chen, Effect of amorphous FeS semiconductor on the corrosion behavior of pipe steel in H_2S-containing environments, Ind. Eng. Chem. Res. 55 (41) (2016) 10932–10940.
[33] E. Wallaert, T. Depover, I. De Graeve, K. Verbeken, FeS corrosion products formation and hydrogen uptake in a sour environment for quenched & tempered steel, Metals 8 (1) (2018) 62.
[34] M.C. Folena, J.A. da Cunha Ponciano, Assessment of hydrogen embrittlement severity of an API 5LX80 steel in H_2S environments by integrated methodologies, Eng. Fail. Anal. 111 (2020) 104380.
[35] C. Zhou, S. Zheng, C. Chen, G. Lu, The effect of the partial pressure of H_2S on the permeation of hydrogen in low carbon pipeline steel, Corros. Sci. 67 (2013) 184–192.
[36] F. Huang, P. Cheng, X. Zhao, J. Liu, Q. Hu, Y.F. Cheng, Effect of sulfide films formed on X65 steel surface on hydrogen permeation in H_2S environments, Int. J. Hydrogen Energy 42 (7) (2017) 4561–4570.
[37] C. Zhou, B. Fang, J. Wang, S. Hu, B. Ye, Y. He, J. Zheng, L. Zhang, Effect of interaction between corrosion film and H_2S/CO_2 partial pressure ratio on the hydrogen permeation in X80 pipeline steel, Corros. Eng. Sci. Technol. 55 (5) (2020) 392–399.
[38] S. Zheng, C. Zhou, P. Wang, C. Chen, L. Chen, Effects of the temperature on the hydrogen permeation behaviours of l360ncs pipeline steel in 1MPa H_2S environments, 2013.
[39] S. Karimi, I. Taji, T. Hajilou, A. Barnoush, R. Johnsen, Evaluation of the cementite morphology influence on the hydrogen induced crack nucleation and propagation path in carbon steels, Int. J. Hydrogen Energy 47 (30) (2022) 14121–14129.
[40] A.S. for Testing, Materials, Standard Practice for the Preparation of Substitute Ocean Water, ASTM International, 2013.
[41] S. Navabzadeh Esmaeely, Y.-S. Choi, D. Young, S. Nešić, Effect of calcium on the formation and protectiveness of iron carbonate layer in CO_2 corrosion, Corrosion 69 (9) (2013) 912–920.
[42] A. Drexler, T. Depover, K. Verbeken, W. Ecker, Model-based interpretation of thermal desorption spectra of Fe-C-Ti alloys, J. Alloys Compd. 789 (2019) 647–657.
[43] H.E. Kissinger, Reaction kinetics in differential thermal analysis, Anal. Chem. 29 (11) (1957) 1702–1706.
[44] J. Lee, J.Y. Lee, Hydrogen trapping in AISI 4340 steel, Metal Sci. 17 (9) (1983) 426–432.
[45] F. Von Zeppelin, M. Haluška, M. Hirscher, Thermal desorption spectroscopy as a quantitative tool to determine the hydrogen content in solids, Thermochim. Acta 404 (1–2) (2003) 251–258.
[46] M.D. Abràmoff, P.J. Magalhães, S.J. Ram, Image processing with imagej, Biophoton. Int. 11 (7) (2004) 36–42.
[47] Y.A. Du, J. Rogal, R. Drautz, Diffusion of hydrogen within idealized grains of bcc Fe: A kinetic Monte Carlo study, Phys. Rev. B 86 (17) (2012) 174110.

[48] Y.A. Du, L. Ismer, J. Rogal, T. Hickel, J. Neugebauer, R. Drautz, First-principles study on the interaction of H interstitials with grain boundaries in α-and γ-Fe, Phys. Rev. B 84 (14) (2011) 144121.
[49] D. Jiang, E.A. Carter, Diffusion of interstitial hydrogen into and through bcc Fe from first principles, Phys. Rev. B 70 (6) (2004) 064102.
[50] K. Verbeken, Analysing hydrogen in metals: bulk thermal desorption spectroscopy (TDS) methods, in: Gaseous Hydrogen Embrittlement of Materials in Energy Technologies, Elsevier, 2012, pp. 27–55.
[51] M. Pinson, L. Claeys, H. Springer, V. Bliznuk, T. Depover, K. Verbeken, Investigation of the effect of carbon on the reversible hydrogen trapping behavior in lab-cast martensitic FeC steels, Mater. Charact. 184 (2022) 111671.
[52] A. Kahyarian, B. Brown, S. Nešić, Electrochemistry of CO2 corrosion of mild steel: effect of CO2 on cathodic currents, Corrosion 74 (8) (2018) 851–859.
[53] C. De Waard, D. Milliams, Carbonic acid corrosion of steel, Corrosion 31 (5) (1975) 177–181.
[54] B. Linter, G. Burstein, Reactions of pipeline steels in carbon dioxide solutions, Corros. Sci. 41 (1) (1999) 117–139.
[55] S. Nesic, J. Postlethwaite, S. Olsen, An electrochemical model for prediction of corrosion of mild steel in aqueous carbon dioxide solutions, Corrosion 52 (4) (1996) 280–294.
[56] E. Remita, B. Tribollet, E. Sutter, V. Vivier, F. Ropital, J. Kittel, Hydrogen evolution in aqueous solutions containing dissolved CO_2: Quantitative contribution of the buffering effect, Corros. Sci. 50 (5) (2008) 1433–1440.
[57] Y. Li, H. Wang, L. Xie, Y. Liang, G. Hong, H. Dai, MoS_2 nanoparticles grown on graphene: an advanced catalyst for the hydrogen evolution reaction, J. Am. Chem. Soc. 133 (19) (2011) 7296–7299.
[58] M. Truschner, A. Trautmann, G. Mori, The basics of hydrogen uptake in iron and steel, BHM Berg-und Hüttenmännische Monatsh. 166 (9) (2021) 443–449.
[59] Y. Cheng, L. Niu, Mechanism for hydrogen evolution reaction on pipeline steel in near-neutral pH solution, Electrochem. Commun. 9 (4) (2007) 558–562.
[60] C. Plennevaux, J. Kittel, M. Fregonese, B. Normand, F. Ropital, F. Grosjean, T. Cassagne, Contribution of CO_2 on hydrogen evolution and hydrogen permeation in low alloy steels exposed to H_2S environment, Electrochem. Commun. 26 (2013) 17–20.
[61] L. Li, J. Yan, J. Xiao, L. Sun, H. Fan, J. Wang, A comparative study of corrosion behavior of S-phase with AISI 304 austenitic stainless steel in $H_2S/CO_2/Cl^-$media, Corros. Sci. 187 (2021) 109472.
[62] S. Wilhelm, D. Abayarathna, Inhibition of hydrogen absorption by steels in wet hydrogen sulfide refinery environments, Corrosion 50 (02) (1994).
[63] E. Hörnlund, J. Fossen, S. Hauger, C. Haugen, T. Havn, T. Hemmingsen, et al., Hydrogen diffusivities and concentrations in 520 M carbon steel under cathodic protection in 0.5 M NaCl and the effect of added sulphite, dithionite, thiosulphate, and sulphide, Int. J. Electrochem. Sci. 2 (2007) 82–92.
[64] R.D. Kane, M.S. Cayard, Roles of H_2S in the behavior of engineering alloys: a review of literature and experience, in: Corrosion 98, OnePetro, 1998.
[65] R. Kirchheim, Bulk diffusion-controlled thermal desorption spectroscopy with examples for hydrogen in iron, Metall. Mater. Trans. A 47 (2) (2016) 672–696.
[66] Y. Amemiya, N. Nakada, S. Morooka, M. Kosaka, M. Kato, Dynamic accommodation of internal stress and selection of crystallographic orientation relationship in pearlite, ISIJ Int. 62 (2) (2022) 282–290.
[67] R. Silverstein, O. Sobol, T. Boellinghaus, W. Unger, D. Eliezer, Hydrogen behavior in SAF 2205 duplex stainless steel, J. Alloys Compd. 695 (2017) 2689–2695.
[68] A. Laureys, L. Claeys, M. Pinson, T. Depover, K. Verbeken, Thermal desorption spectroscopy evaluation of hydrogen-induced damage and deformation-induced defects, Mater. Sci. Technol. 36 (13) (2020) 1389–1397.
[69] W. Choo, J.Y. Lee, Thermal analysis of trapped hydrogen in pure iron, Metall. Trans. A 13 (1) (1982) 135–140.
[70] D.P. Escobar, K. Verbeken, L. Duprez, M. Verhaege, Evaluation of hydrogen trapping in high strength steels by thermal desorption spectroscopy, Mater. Sci. Eng. A 551 (2012) 50–58.
[71] E. Dabah, V. Lisitsyn, D. Eliezer, Performance of hydrogen trapping and phase transformation in hydrogenated duplex stainless steels, Mater. Sci. Eng. A 527 (18–19) (2010) 4851–4857.
[72] K. Kawakami, T. Matsumiya, Ab-initio investigation of hydrogen trap state by cementite in bcc-Fe, ISIJ Int. 53 (4) (2013) 709–713.
[73] G.-W. Hong, J.-Y. Lee, The interaction of hydrogen and the cementite-ferrite interface in carbon steel, J. Mater. Sci. 18 (1) (1983) 271–277.
[74] W. Choo, J.Y. Lee, Hydrogen trapping phenomena in carbon steel, J. Mater. Sci. 17 (7) (1982) 1930–1938.
[75] K. Takai, R. Watanuki, Hydrogen in trapping states innocuous to environmental degradation of high-strength steels, ISIJ Int. 43 (4) (2003) 520–526.
[76] J.S. Kim, Y.H. Lee, D.L. Lee, K.-T. Park, C.S. Lee, Microstructural influences on hydrogen delayed fracture of high strength steels, Mater. Sci. Eng. A 505 (1–2) (2009) 105–110.
[77] W.M. Robertson, A.W. Thompson, Permeation measurements of hydrogen trapping in 1045 steel, Metall. Trans. A 11 (4) (1980) 553–557.
[78] P.K. Katiyar, S. Misra, K. Mondal, Corrosion behavior of annealed steels with different carbon contents (0.002, 0.17, 0.43 and 0.7% C) in freely aerated 3.5% NaCl solution, J. Mater. Eng. Perform. 28 (7) (2019) 4041–4052.
[79] K. Godbole, K. Mondal, Influence of salinity, total dissolved solids, conductivity, and pH on corrosion behavior of different morphologies of pearlitic steels, J. Mater. Eng. Perform. (2022) 1–11.
[80] R. Cabrera-Sierra, N. Batina, I. González, Electrochemical characterization of pearlite phase oxidation of 1018 carbon steel in a borate medium using ECSTM technique, J. Electrochem. Soc. 152 (12) (2005) B534.
[81] E. Anyanwu, B. Brown, M. Singer, Effect of iron carbide on the morphology and protectiveness of iron sulfide layer, in: Corrosion 2020, OnePetro, 2020.
[82] S. Silva, A. Silva, J.P. Gomes, Hydrogen embrittlement of API 5L X65 pipeline steel in CO_2 containing low H_2S concentration environment, Eng. Fail. Anal. 120 (2021) 105081.
[83] M. Kappes, G. Frankel, N. Sridhar, R. Carranza, Reaction paths of thiosulfate during corrosion of carbon steel in acidified brines, J. Electrochem. Soc. 159 (4) (2012) C195.